



## Swift heavy ion-induced amorphization of CaZrO<sub>3</sub> perovskite

Maik Lang<sup>a,\*</sup>, Fuxiang Zhang<sup>a</sup>, Weixing Li<sup>a</sup>, Daniel Severin<sup>b</sup>, Markus Bender<sup>b</sup>,  
Siegfried Klaumünzer<sup>c</sup>, Christina Trautmann<sup>b</sup>, Rodney C. Ewing<sup>a</sup>

<sup>a</sup> Department of Earth & Environmental Sciences and Materials Science & Engineering, University of Michigan, Ann Arbor, MI 48109, USA

<sup>b</sup> GSI Helmholtzzentrum für Schwerionenforschung GmbH, 64291 Darmstadt, Germany

<sup>c</sup> Department Spallationsforschung mit Neutronen, Helmholtz-Zentrum Berlin für Materialien und Energie GmbH, 14109 Berlin, Germany

### ARTICLE INFO

#### Article history:

Received 23 August 2011

Received in revised form 29 November 2011

Available online 2 January 2012

#### Keywords:

Swift heavy ion irradiation

Perovskite

X-ray diffraction

### ABSTRACT

Perovskite, ABO<sub>3</sub>, structures are an important class of ceramics with a large variety of derivative structure-types (cubic, tetragonal, hexagonal, orthorhombic, and rhombohedral). Radiation damage in perovskites is of interest due to their potential as actinide waste forms and to understand radiation effects in uranium- and thorium-bearing phases. Powder CaZrO<sub>3</sub> perovskite was irradiated with 940-MeV Au ions up to  $1.5 \times 10^{13}$  ions/cm<sup>2</sup>. Changes in the crystal structure were followed *in situ* as function of fluence by means of a sequence of X-ray diffraction (XRD) measurements. Ion-induced amorphization is evidenced by a decrease in diffraction intensity and an increase in diffuse scattering. Based on XRD measurements, as well as transmission electron microscopy (TEM), CaZrO<sub>3</sub> is completely amorphized at a fluence of  $1.5 \times 10^{13}$  ions/cm<sup>2</sup>. From the evolution of the integrated XRD-maxima intensities with fluence, the diameter of the amorphous tracks is estimated to be  $6.0 \pm 0.6$  nm, which is independently confirmed by bright-field TEM images:  $6.7 \pm 0.4$  nm. Changes in the positions of diffraction maxima may be caused by at least two processes. Broadening of the diffraction maxima is analyzed using a Williamson–Hall plot. Strain-induced broadening is the dominant process.

© 2011 Elsevier B.V. All rights reserved.

### 1. Introduction

The ABO<sub>3</sub> perovskite structure-type has a wide variety of technological applications, as sensors and catalysts [1], solid-state proton conductors [2], multiferroics [3], substrates for superconductors [4,5], and nuclear waste forms for fission products and actinides [6]. The very different physical and chemical properties of perovskite materials reflect their large structural flexibility. Many different chemical compositions can be synthesized due to a variety of possible combinations of charge for the A- and B-site cations. The mineral name perovskite has the composition: CaTiO<sub>3</sub> which is orthorhombic [7]. The perovskite structure (*Pbnm*) is derived from the ideal cubic perovskite (*Pm $\bar{3}$ m*) by tilting the corner-sharing BO<sub>6</sub> octahedra [7,8]. The larger A-site cations are located within cages created by the octahedral framework of smaller B-cations. The degree of distortion from the ideal cubic structure is determined by the amount of tilting of BO<sub>6</sub> octahedra, which depends on the relative size of the A- and B-site cations. CaZrO<sub>3</sub> has one of the largest structural distortions among the perovskite compositions (Fig. 1).

Titanium- and strontium-based perovskites are of particular interest due to their potential as materials for the immobilization

and disposal of actinides. Perovskite is one of the main phases in SYNROC, a polyphase, Ti-based nuclear waste form [9–12]. The effect of alpha-decay events in CaTiO<sub>3</sub> and SrTiO<sub>3</sub> perovskite has been studied via irradiation experiments [12–25] and by characterizing natural radiation damage in uranium- and thorium-bearing compounds [26]. Irradiation experiments exposing different titanate, tantalate and niobate perovskites to 800-keV Kr<sup>+</sup>, Xe<sup>+</sup>, and Ne<sup>+</sup> ions revealed an enhanced radiation stability with the decreasing mass of A- and B-site cations [12]. For the CaTiO<sub>3</sub> and SrTiO<sub>3</sub> compositions, ion-induced amorphization was evident only above a critical energy-loss (*dE/dx*) threshold [12]. The radiation tolerance of different perovskites with respect to the underlying energetics of defect formation has also been the subject of classical and quantum-mechanical simulations [27,28]. These studies showed that the resistance to radiation depends on the structure type, with orthorhombic perovskite being one of the least resistant to radiation damage [27].

In this study, CaZrO<sub>3</sub> perovskite was irradiated with 940-MeV Au ions and analyzed by *in situ* X-ray diffraction (XRD) and transmission electron microscopy (TEM). Such projectiles lose their energy almost entirely through ionization and excitation processes (electronic *dE/dx*). Up to now, zirconate perovskites have only been subjected to gamma radiation [29], low-energy light ions [29,30] and neutrons [31]. The general information on the response of perovskite under ion irradiation has focused mainly on titanate

\* Corresponding author.

E-mail address: [mklang@umich.edu](mailto:mklang@umich.edu) (M. Lang).

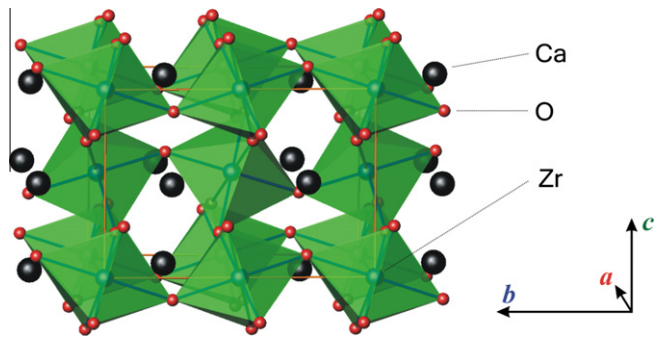


**Fig. 1.** Crystal structure of orthorhombic  $\text{CaZrO}_3$  ( $Pcmn$ ). The corner-sharing  $\text{ZrO}_6$  octahedral framework forms cavities filled with Ca atoms. The unit-cell volume and unit-cell parameters of the initial  $\text{CaZrO}_3$  powder were determined from the XRD pattern by a refinement-like fit:  $V_0 = 257.8(1) \text{ \AA}^3$ ,  $a = 5.588(1) \text{ \AA}$ ,  $b = 8.015(2) \text{ \AA}$  and  $c = 5.756(1) \text{ \AA}$ .

perovskites and low-energy ions [12–25], the knowledge of the effects of swift heavy ion irradiation in the electronic stopping regime is limited [32–34].

## 2. Experimental

A powder sample of  $\text{CaZrO}_3$  was synthesized by solid state reaction of  $\text{CaO}$  and  $\text{ZrO}_2$  in an oxygen atmosphere at  $1300 \text{ }^\circ\text{C}$  for several days. The two components were repeatedly intermixed, pressed into pellets (diameter  $1.25 \text{ cm}$ , thickness  $\sim 2 \text{ mm}$ ), and subsequently sintered for  $24 \text{ h}$  at  $1200 \text{ }^\circ\text{C}$ . Perovskite oxides fabricated under such conditions have a typical grain size of a few microns, and the porosity is estimated to be between 25 and 50%. The starting material was characterized by means of XRD confirming the orthorhombic perovskite structure. The pellets were glued with epoxy resin onto single crystal silicon substrates (to minimize background radiation for XRD measurements), which were attached to copper sample holders. The irradiation experiments were completed with  $940\text{-MeV}$  Au ions at the new M2 beamline at the UNILAC accelerator of GSI (Darmstadt, Germany). With a theoretical density of  $4.62 \text{ g/cm}^3$  for  $\text{CaZrO}_3$  perovskite, the ion range was calculated to  $35 \text{ }\mu\text{m}$ . The beam spot size was  $2.25 \text{ cm}^2$ , thus exposing the entire sample. The ion flux was between  $0.5 \times 10^9$  and  $2 \times 10^9 \text{ ions/cm}^2\text{s}$  which is sufficiently low to avoid macroscopic sample heating. The room temperature irradiations were performed in steps of  $1 \times 10^{12} \text{ ions/cm}^2$  up to a fluence of  $8 \times 10^{12} \text{ ions/cm}^2$  with two additional exposures at  $1 \times 10^{13} \text{ ions/cm}^2$  and  $1.5 \times 10^{13} \text{ ions/cm}^2$ . During interruptions to the irradiation, the structure of the powder material was analyzed by XRD measurements *in situ* at the beamline. The instrument is a standard 4-circle X-ray diffractometer ( $\text{Cu-K}\alpha$ ) operating in vacuum and equipped with a position-sensitive detector. The X-ray tube was operated in point focus geometry. XRD patterns were recorded between  $20^\circ$  and  $60^\circ$  using symmetric Bragg scattering with an exposure time of  $100 \text{ s}$  up to  $7 \times 10^{12} \text{ ions/cm}^2$  and  $200 \text{ s}$  for the last three irradiation steps. The instrumental resolution in the scattering angle  $2\theta$ ,  $\beta_{\text{inst}}$ , was determined by means of a crystalline  $\text{Al}_2\text{O}_3$  sample (standard reference material 1976a from NIST) and approximated by

$$\beta_{\text{inst}}^2 = 2.89 \times 10^{-4} + 3.05 \times 10^{-7} \tan \theta + 5.18 \times 10^{-6} \tan^2 \theta,$$

where  $\beta_{\text{inst}}$  is given in rad and refers to the full-width at half-maximum (FWHM). Even at the largest scattering angle of  $2\theta = 60^\circ$ , about 90% of the scattered intensity originated from the first  $10 \text{ }\mu\text{m}$  below the specimen surface. Within this range, the electronic  $dE/dx$  of the energetic gold ions was within  $35\text{--}36 \text{ keV/nm}$  nearly constant, and the nuclear  $dE/dx$  was well below 0.5% of the total energy loss (SRIM 2008). A synchrotron-based characterization

of radiation-induced amorphization is superior in terms of signal-to-background ratio [35]; however, measurements at the M2 X-ray diffractometer beamline at GSI allow for a larger number of fluence steps. All diffraction profiles were analyzed with the software DataLab by fitting Gaussian curves to the main diffraction maxima. The use of Gaussian line profiles will be discussed below (see also remark [47]). Peak position, FWHM, intensity and area were determined for each irradiation step. Refinement-like fitting of the full XRD patterns of the starting material using the software FullProf [36] yielded a unit cell volume of  $V_0 = 257.8(1) \text{ \AA}^3$  with  $a = 5.588(1) \text{ \AA}$ ,  $b = 8.015(2) \text{ \AA}$  and  $c = 5.756(1) \text{ \AA}$  in good agreement with previously published results. Finally, samples from irradiations at two different fluences were subsequently investigated by TEM (JEOL 2010F) obtaining bright-field images, electron diffraction patterns and energy dispersive X-ray spectra (EDAX). In order to image single ion tracks without overlap, one pellet was limited to a fluence of  $1 \times 10^{11} \text{ ions/cm}^2$ . The second TEM sample was prepared from the pellet exposed to the highest fluence after the entire irradiation series ( $1.5 \times 10^{13} \text{ ions/cm}^2$ ). In both cases, a few grains were carefully scraped off from the sample surface and dispersed onto a holey-carbon grid for TEM examination.

## 3. Results and discussion

A series of diffraction patterns of  $\text{CaZrO}_3$  perovskite before and after irradiation are shown in Fig. 2. The main crystalline diffraction maxima (101, 020, 200, 121, 002, 202, 040; see unirradiated sample in Fig. 2 for indexing) decrease strongly with irradiation, accompanied by pronounced broadening. Beginning with a fluence of  $3 \times 10^{12} \text{ ions/cm}^2$ , ion-induced amorphization is evident. The interaction of X-rays with amorphous domains is characterized by a broad maximum in the two theta region of the most intense

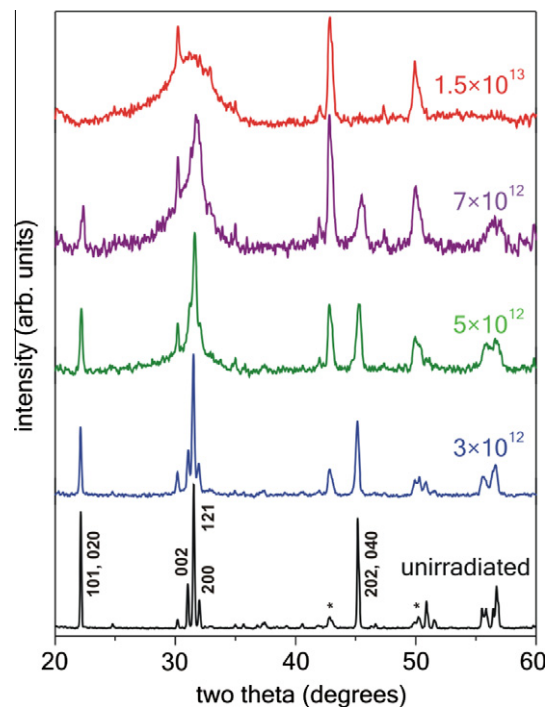


**Fig. 2.** Series of XRD patterns of  $\text{CaZrO}_3$  perovskite before and after irradiation with  $940\text{-MeV}$  Au ions at different fluences. Amorphization with increasing fluence is evident by the decrease in intensity of the diffraction peaks concurrent with the growth of a diffuse background intensity ( $\sim 30^\circ$ ). XRD contributions from the copper sample holder are labeled with an asterisk (\*). XRD pattern of the unirradiated sample is indexed. Note, the 101 and 020 (202 and 040) diffraction maxima overlap and appear as one single peak.

diffraction maxima of the crystalline phase [37]. With increasing fluence (bottom to top in Fig. 2), the broad, amorphous “peak” grows systematically and is the dominant feature in the pattern at the maximum fluence with no indication of crystalline CaZrO<sub>3</sub> diffraction maxima. Two prominent sharp peaks at  $1.5 \times 10^{13}$  ions/cm<sup>2</sup> at  $2\theta = \sim 43^\circ$  and  $\sim 50^\circ$  are due to the interaction of the copper sample holder with the X-ray beam when its spot size exceeds the sample dimension (see caption of Fig. 2). The remaining peaks are probably due to double Bragg scattering (Umweganregung) from the single crystal substrate. These diffraction maxima are present in all patterns, but are particularly prominent at higher fluences for which the overall sample intensity is greatly reduced by the amorphization process. TEM characterization independently confirms completion of the radiation-induced crystalline-to-amorphous phase transformation at the highest fluence. Bright-field images and selected area electron diffraction patterns (both not presented) indicate only the presence of amorphous material, i.e., based on uniform contrast without any evident crystalline contribution to the diffraction pattern and diffuse scattering from the amorphous domains.

The crystalline and amorphous contributions were quantified by a peak-fitting procedure at each irradiation step. Above a fluence of  $2 \times 10^{12}$  ions/cm<sup>2</sup>, all patterns were additionally deconvoluted in the two-theta region between  $25^\circ$  and  $35^\circ$  into four different contributions consisting of three crystalline peaks (002, 121, 200) and a diffuse broad peak from the amorphous domains of the sample (Fig. 2). This procedure is described in detail elsewhere [37]. Note, the diffraction maximum from the sample holder, at  $\sim 30^\circ$ , was also considered in the deconvolution/fitting process. Fits to the 101, 020 and 202, 040 diffraction maxima (see Fig. 2 for indexing) were directly applied without deconvolution due to the absence of the diffuse scattering from the amorphous domains and no peak overlap. With increasing fluence, the normalized area of the crystalline sample fraction, shown in Fig. 3 by the relative areas of the 101, 020 diffraction maxima (one peak in Fig. 2), decreases quickly with increasing irradiation. The loss of long-range XRD periodicity due to radiation damage and amorphization is the main cause for this decrease [38,39]. The decrease of the relative area  $n_c(\Phi) = C(\Phi)/C_{\max}$  as function of irradiation fluence can be well described by an exponential expression [40]:

$$n_c(\Phi) = 100 \cdot e^{-(\sigma \cdot \Phi)}, \quad (1)$$

where  $C(\Phi)$  represents the measured crystalline peak area at the fluence  $\Phi$  and  $C_{\max}$  the maximum value prior to irradiation,

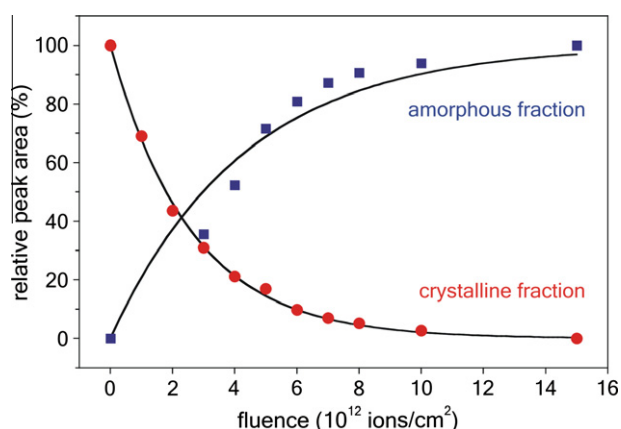


**Fig. 3.** Relative peak area of amorphous (diffuse diffraction maximum at  $\sim 30^\circ$ ) and crystalline (101, 020 diffraction maxima) fraction as a function of increasing fluence. The curves are fits to the data by Eqs. (1) and (2) and provide the cross-sections for amorphous tracks.

$n_c(\Phi) = 100\%$ . Fitting Eq. (1) to the data points of the crystalline fraction (filled circles in Fig. 3) allowed for the estimate of the cross-section for the decrease of crystalline maxima,  $\sigma = 38.6 \text{ nm}^2$ , and the corresponding effective track diameter,  $d = 7.0 \text{ nm}$ , by assuming cylindrical track geometry ( $\sigma = \pi \cdot (d/2)^2$ ). The identical procedure was applied for several other crystalline diffraction peaks, yielding similar values (002: 5.4 nm; 121: 5.8 nm; 200: 6.4 nm; 202, 040: 5.9 nm).

Concurrent to the exponential decrease of the crystalline peak area, the normalized area of the broad amorphous peak,  $n_A(\Phi) = A(\Phi)/A_{\max}$ , grows linearly in the initial stage and finally reaches saturation at higher fluences (Fig. 3). This behavior is described by an exponential Eq. (2) based on a direct-impact model [40].

$$n_A(\Phi) = 100 \cdot (1 - e^{-(\sigma \cdot \Phi)}), \quad (2)$$

where  $A(\Phi)$  represents the measured peak area at the fluence  $\Phi$  and  $A_{\max}$  the maximum value for complete amorphization  $n_A(\Phi) = 100\%$ . The amorphization cross-section per incident ion is given by  $\sigma$ . In the direct-impact model, amorphization is described by the accumulation of individual amorphous tracks. At larger fluences, tracks begin to overlap, and the increase in amorphous fraction becomes sub-linear. Fitting Eq. (2) to the XRD data of the amorphous fraction (filled squares in Fig. 3) yields the amorphization cross-section,  $\sigma = 23.3 \text{ nm}^2$ , and the corresponding effective track diameter,  $d = 5.4 \text{ nm}$ , of the amorphous track zone. Direct-impact amorphization was not observed within the nuclear  $dE/dx$  regime of keV–MeV ions in SrTiO<sub>3</sub> perovskite, but defect-stimulated amorphization by overlaps of damage cascades [23,24]. Deviations from Eq. (2) in Fig. 3 can be ascribed to the low-intensity of the diffuse amorphous diffraction maximum, particularly for low fluences, and related uncertainties in the peak-fitting procedure. However, the cross-section for the increasing amorphous fraction is somewhat smaller than the corresponding decreasing crystalline fraction (Fig. 3). This trend can be understood in terms of the specific material modifications contributing to both cross-sections [35]. The ingrowth of the diffuse amorphous peak is only caused by the amorphous phase; whereas, highly defective and strained sample regions may also contribute to the larger cross-section of the decreasing intensity of peaks from crystalline domains. A defect-rich, yet crystalline, track halo surrounding individual amorphous track cores can account for the smaller amorphization cross-section. Such a halo may also be responsible for the small deviation of the ingrowth of amorphous phase (filled squares in Fig. 3) with respect to the direct-impact model (fit of Eq. (2) in Fig. 3). Concerning the uncertainty in the XRD measurements, only one pattern was recorded at each irradiation step. Additionally, the error in the peak-fitting procedure is not unambiguously determined. Thus, a mean diameter and sigma were established for the XRD data by averaging over all values obtained from different diffraction maxima:  $6.0 \pm 0.6 \text{ nm}$ .

A bright-field TEM image of the sample irradiated at  $1 \times 10^{11}$  ions/cm<sup>2</sup> is shown in Fig. 4. Ion tracks are apparent due to their different contrast with respect to the surrounding matrix. The number of tracks is in agreement with the irradiation fluence (slightly larger). Thus, in CaZrO<sub>3</sub> each impinging ion creates an individual track, supporting the use of the single-impact model to fit the XRD data. Size measurements of 20 tracks yield a mean diameter and sigma of  $d = (6.7 \pm 0.4) \text{ nm}$ . The track size distribution is rather narrow, which is attributed to cylindrical track morphology. The track diameters deduced from TEM and XRD are in good agreement and indicate that CaZrO<sub>3</sub> perovskite has an increased resistance to swift heavy ion irradiation as compared with other ceramics, e.g., Gd<sub>2</sub>Ti<sub>2</sub>O<sub>7</sub> pyrochlore ( $d = 9.2 \pm 0.9 \text{ nm}$ , <sup>129</sup>Xe ions, 1.4 GeV,  $dE/dx = 28.5 \text{ keV/nm}$ , [35]) and Ca<sub>10</sub>(PO<sub>4</sub>)<sub>6</sub>(OH, F, Cl)<sub>2</sub> apatite ( $d = 9.0 \pm 1.0 \text{ nm}$ , <sup>197</sup>Au ions, 2.2 GeV,  $dE/dx = 26 \text{ keV/nm}$ ,

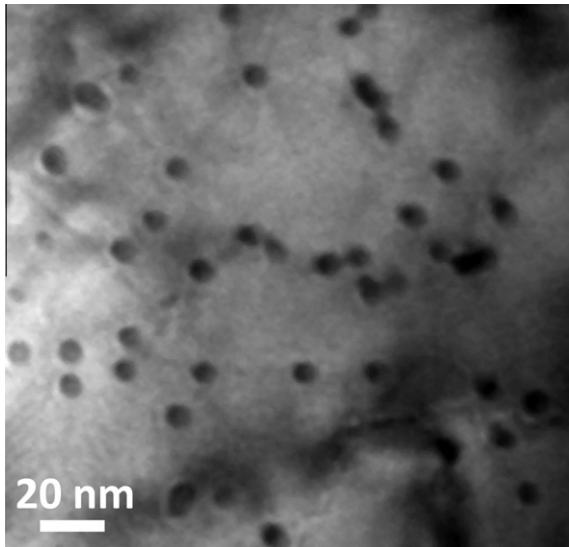


**Fig. 4.** TEM bright-field image of  $\text{CaZrO}_3$  perovskite after irradiation with  $1 \times 10^{11} \text{ cm}^{-2}$  Au ions of energy 940 MeV. Amorphous tracks of diameter  $6.7 \pm 0.4 \text{ nm}$  are visible by concentric contrast variations.

[41,42]). The higher radiation tolerance of the perovskite structure was also evident in studies on natural and ion-induced radiation damage in uranium- and thorium-bearing minerals suggesting that calcium-titanate perovskite is more stable than pyrochlore or zirconolite [25]. The enhanced structural stability of  $\text{CaZrO}_3$  might be related to the relatively small mass of the A-site cation, as suggested by a previous ion-beam investigation of different perovskite compositions [12]. The predicted lower radiation performance for the orthorhombic structured perovskite as compared with  $\text{A}_2\text{B}_2\text{O}_7$  pyrochlore [27] could not be confirmed for swift heavy

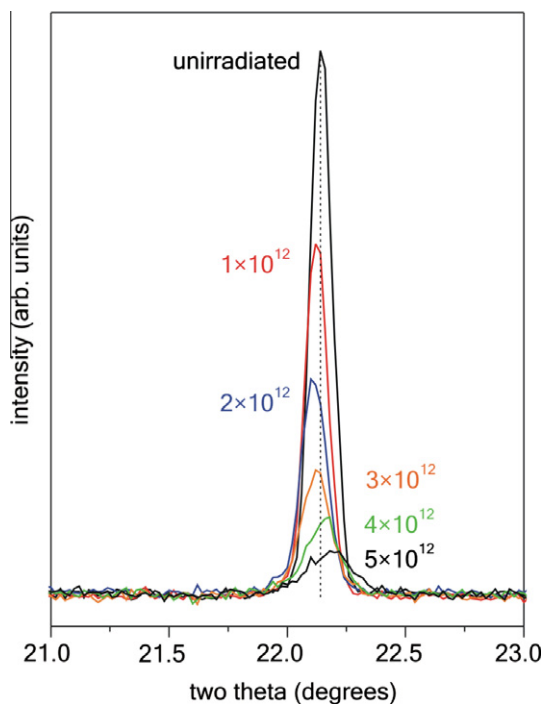


**Fig. 5.** Detailed view of 101 and 020 diffraction maximum for starting material and first 5 irradiation fluences up to  $5 \times 10^{12} \text{ ions/cm}^2$ . With accumulating ion bombardment, the peak intensity decreases, whereas the peak width increases. The position of the diffraction maximum shifts first to lower and then to higher  $2\theta$ .

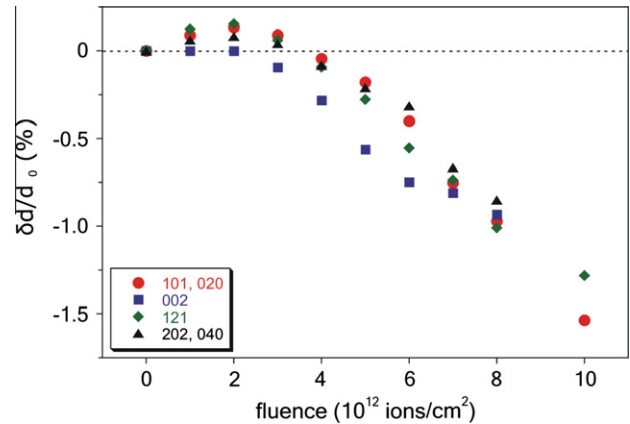


**Fig. 6.** Relative shifts of the interplanar distances,  $\delta d/d_0 = -\delta\theta/\tan\theta$ , for the most prominent diffraction maxima (101, 020, 002, 121, 202, 040) as a function of ion fluence. The initial interplanar distance  $d_0$  denotes to prior to irradiation.

ion irradiation, even though  $\text{CaZrO}_3$  has the most distorted structure of a wide range of perovskite compositions [43]. For a more detailed comparison, the  $dE/dx$  thresholds for track formation must be compared in the different ceramics.

The 101, 020 peak (two overlapping peaks, see Fig. 2 for indexing) of the unirradiated sample and its evolution under irradiation up to  $5 \times 10^{12} \text{ ions/cm}^2$  is shown in Fig. 5, illustrating the decrease in peak intensity and pronounced broadening. The peak position with respect to the unirradiated sample (dashed line in Fig. 5) is complex. The relative changes of the interplanar distances,  $\delta d/d_0 = -\delta\theta/\tan\theta$ , are calculated from Bragg's law and are displayed for the most prominent peaks as a function of fluence in Fig. 6. The lattice plane distance prior to irradiation,  $d_0$ , is given by  $1/d_0^2 = h^2/a^2 + k^2/b^2 + l^2/c^2$  with the Miller indices  $h$ ,  $k$  and  $l$ . Mechanisms which can contribute to changes in interplanar distances after irradiation are: (i) generation of defects in the crystalline matrix or by compositional changes due to radiolysis, and (ii) the build-up of mechanical stresses caused by the formation of an amorphous phase with a concomitant volume change or by bombardment-induced pore shrinkage of the porous powder. The complex shift of interplanar distances with fluence (Fig. 6) is indicative of at least two different operative mechanisms. The determination and separation of (i) and (ii) is, in principle, possible with a four-circle diffractometer but requires the knowledge of the X-ray elastic constants which are presently unknown for orthorhombic  $\text{CaZrO}_3$ . No compositional changes were evident by the TEM analysis (EDAX) at the level of a few atomic percent; however,

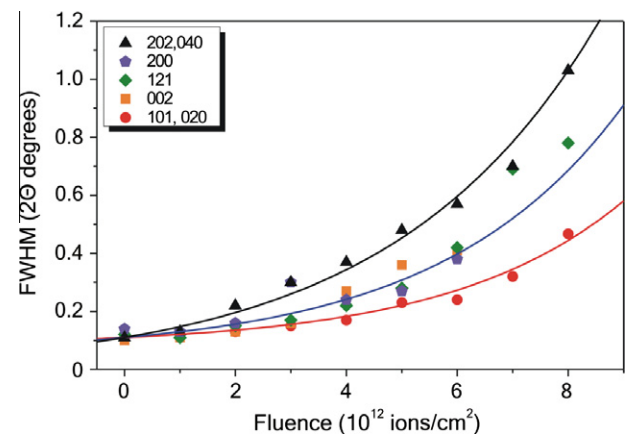


**Fig. 7.** Full widths at half maximum (FWHM) in  $2\theta$  in degrees of the most intense Bragg diffraction maxima. The curves are drawn to guide the eye.

compositional changes below this limit cannot be excluded. Interestingly, at fluences  $> 4 \times 10^{12}$  ions/cm<sup>2</sup>,  $\delta d/d_0$  is negative (Fig. 6). If this quantity is interpreted as an elastic strain caused by an in-plane stress, this stress must be tensile; an observation which is in conflict with the typical volume expansion by defect generation [44], by amorphization and ion hammering of the amorphous phase. However, swift heavy ion-induced efficient pore shrinkage of porous CaZrO<sub>3</sub> would result in a tensile stress and explain the observed effect. It should be noted that the pellets were prepared with a hand press operating at low pressure. Thus, the actual density of the powdered samples was significantly lower than the calculated value (estimated on the order of 75%).

The experimentally determined FWHM of the five main diffraction maxima versus ion fluence is shown in Fig. 7, displaying significant increase for all peaks. For Gaussian line profiles of the Bragg diffractions, the Williamson–Hall formula is given by

$$\beta^2 = g \left\{ \left( \frac{K\lambda}{D \cos \theta} \right)^2 + 16\varepsilon^2 \tan^2 \theta \right\}$$

where the line width  $\beta$  is corrected for the instrumental resolution by  $\beta^2 = \text{FWHM}^2 - \beta_{\text{inst}}^2$ . The constant  $g = (4 \ln 2)/\pi$  converts integral line widths into FWHM values.  $\lambda$  is the X-ray wavelength,  $D$  the (weighted) average crystallite size proportional to the cubic root of the crystallite volume, and  $\varepsilon$  is a measure for the strain fluctuations, sometimes also denoted as microstrains. The shape of the crystallites and their orientation relative to the X-ray scattering vector is taken into account by the Scherrer constant  $K$ . With increasing ion fluence, the amorphous tracks overlap and  $D$  decreases. One might be tempted to ascribe the increase in  $\beta$  to the decrease in  $D$ . However, in the specific geometry of this work, the scattering vector coincided with the direction of the incident ion beam and, for a perfectly aligned setup and perfectly parallel ion tracks, the crystallite size in this direction remains unaffected and is of the order of a few micrometers (cf. Section 2). Theoretically, for prismatic crystallites with their lengths much larger than their diameters and all prism axes parallel to the X-ray scattering vector,  $K$  is close to zero [45,46]. In fact, plotting  $\beta^2 \cos^2 \theta$  versus  $\sin^2 \theta$  (see Fig. 8) reveals that  $K\lambda/D$  is zero within the experimental uncertainties for all fluences. Hence, the measured increase in  $\beta$  is essentially due to microstrains [47]. The quantity  $\varepsilon$  is plotted in Fig. 9 and is almost linear in ion fluence. It should be noted that close to complete amorphization, i.e., for a fluence above  $8 \times 10^{12}$  ions/cm<sup>2</sup>,  $\varepsilon$  approaches the elastic strain limit, which is between 0.2 and 0.3 for ionic ceramics [48].

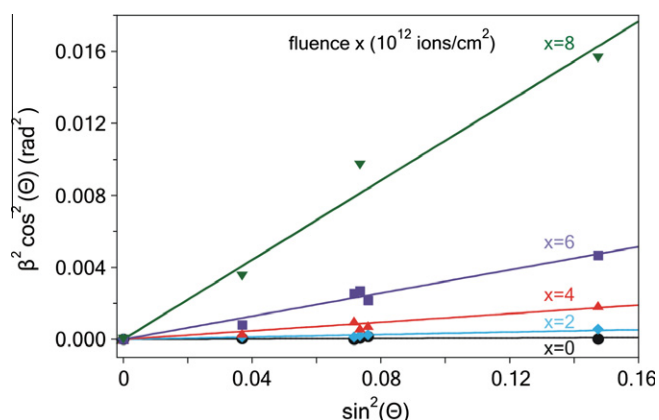


Fig. 8. Williamson–Hall plot for the most intense Bragg diffraction maxima for 5 different fluences. Note, that the straight lines intersect the ordinate close to the origin indicating negligible crystallite size broadening. This effect is due to the specific geometry used during irradiation and measurement (see text for details).

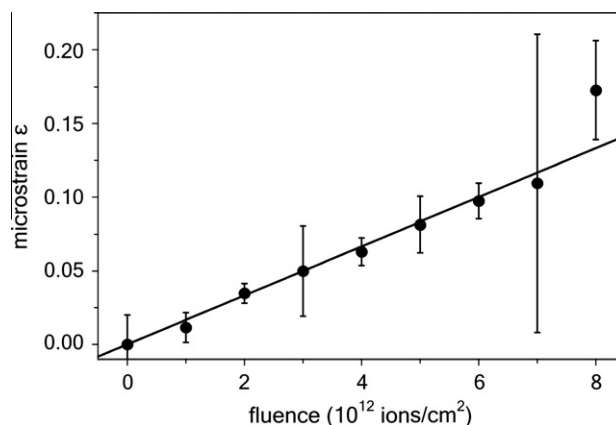


Fig. 9. Fluence dependence of microstrain,  $\varepsilon$ , as derived from slopes in Fig. 8 by applying the Williamson–Hall formula as function of fluence.

#### 4. Conclusions

CaZrO<sub>3</sub> was irradiated with 940-MeV Au ions to a maximum fluence of  $1.5 \times 10^{13}$  ions/cm<sup>2</sup>. By means of *in situ* XRD measurements, ion-induced amorphization was followed as a function of increasing fluence. Based on the diffraction data, individual tracks had a calculated diameter of  $6.0 \pm 0.6$  nm. This was independently confirmed by direct TEM measurements, giving an observed size of  $6.7 \pm 0.4$  nm. The shifts of the position of the diffraction peaks are complex and indicate contributions from several processes. Microstrains approach the elastic limit and cause significant peak broadening.

#### Acknowledgment

This work was supported as part of the Materials Science of Actinides, an Energy Frontier Research Center funded by the U.S. Department of Energy, Office of Science, Office of Basic Energy Sciences under Award Number DE-SC0001089.

#### References

- [1] A. Navrotsky, D.J. Weidner, Perovskite: A Structure of Great Interest to Geophysics and Materials Science, American Geophysical Union, 1989.
- [2] E.C.C. de Souza, R. Muccillo, Properties and applications of perovskite proton conductors, Mater. Res. 13 (2010) 385.
- [3] S.L. Swartz, Topics in electronic ceramics, IEEE Trans. Dielectr. Electr. Insul. 25 (1990) 935.
- [4] M. Kawasaki, K. Takahashi, T. Maeda, R. Tsuchiya, M. Shinohara, O. Ishiyama, T. Yonezawa, M. Yoshimoto, H. Koinuma, Atomic control of the SrTiO<sub>3</sub> crystal surface, Science 266 (1994) 1540.
- [5] C. Aruta et al., Structure of superconducting [BaCuO<sub>x</sub>]<sub>2</sub>/[CaCuO<sub>2</sub>]<sub>n</sub> superlattices on SrTiO<sub>3</sub>(001) investigated by X-ray scattering, Phys. Status Solidi A 183 (2001) 353.
- [6] G.R. Lumpkin, Alpha-decay damage and aqueous durability of actinide host phases in natural systems, J. Nucl. Mater. 289 (2001) 136.
- [7] A.M. Glazer, The classification of tilted octahedra in perovskites, Acta Crystallogr., Sect. B 28 (1972) 3384.
- [8] F.D. Bloss, Crystallography and Crystal Chemistry, Mineralogical Society of America, Washington, DC, 1994.
- [9] A.E. Ringwood, S.E. Kesson, N.G. Ware, W. Hibberston, A. Major, Immobilization of high level nuclear reactor wastes in SYNROC, Nature 278 (1979) 219.
- [10] A.E. Ringwood, S.E. Kesson, K.D. Reeve, D.M. Levins, E.J. Ramm, in: W. Lutze, R.C. Ewing (Eds.), Radioactive Waste Forms for the Future, North-Holland, Amsterdam, 1988, p. 233.
- [11] E.R. Vance, M.W.A. Stewart, G.R. Lumpkin, Immobilization of sodium and potassium in SYNROC, J. Mater. Sci. 26 (1991) 2694.
- [12] A. Meldrum, L.A. Boatner, W.J. Weber, R.C. Ewing, Amorphization and recrystallization of the ABO<sub>3</sub> oxides, J. Nucl. Mater. 300 (2002) 242.
- [13] A. Meldrum, L.A. Boatner, R.C. Ewing, Effects of ionizing and displacive irradiation on several perovskite-structure oxides, Nucl. Instrum. Methods B 141 (1998) 347.

- [14] K.L. Smith, G.R. Lumpkin, M.G. Blackford, M. Colella, N.J. Zaluzec, In situ radiation damage studies of  $\text{La}_x\text{Sr}_{1-3x/2}\text{TiO}_3$  perovskites, *J. Appl. Phys.* 103 (2008) 083531.
- [15] F.G. Kariotis, K.A. Gowda, L. Cartz, J.C. Labbe, Damage cross-sections of heavy ions in crystal structures, *J. Nucl. Mater.* 108–109 (1982) 748.
- [16] C.W. White, L.A. Boatner, J. Rankin, M.J. Aziz, Ion implantation and annealing of  $\text{SrTiO}_3$  and  $\text{CaTiO}_3$ , *Mater. Res. Soc. Symp. Proc.* 93 (1987) 9.
- [17] C.W. White, L.A. Boatner, P.S. Sklad, C.J. McHargue, S.J. Pennycook, M.J. Aziz, G.C. Farlow, J. Rankin, Ion implantation and annealing of oxides, *Mater. Res. Soc. Symp. Proc.* 74 (1987) 357.
- [18] C.W. White, L.A. Boatner, P.S. Sklad, C.J. McHargue, J. Rankin, G.C. Farlow, M.J. Aziz, Ion implantation and annealing of crystalline oxides and ceramic materials, *Nucl. Instrum. Methods Phys. Res., Sect. B* 32 (1988) 11.
- [19] J. Rankin, L.A. Boatner, C.W. White, L.W. Hobbs, A cross-sectional TEM study of the effects of annealing conditions on the regrowth of lead-implanted single crystal calcium titanate, *Mater. Res. Soc. Symp. Proc.* 100 (1988) 453.
- [20] J. Rankin, L.W. Hobbs, L.A. Boatner, C.W. White, An in situ annealing study of lead implanted single crystal calcium titanate, *Nucl. Instrum. Methods B* 32 (1988) 28.
- [21] K.L. Smith, M.G. Blackford, G.R. Lumpkin, in: I.G. McKinley, C. McCombie (Eds.), *Scientific Basis for Nuclear Waste Management XXI*, vol. 506, Mater. Res. Soc. Symp. Proc., Materials Research Society, Pittsburgh, PA, 1998, p. 929.
- [22] W.J. Weber, W. Jiang, S. Thevuthasan, R.E. Williford, A. Meldrum, L.A. Boatner, in: G. Borstel, A. Krumins, D. Millers (Eds.), *Defects and Surface-Induced Effects in Advanced Perovskites*, Kluwer Academic, Dordrecht, 2000, p. 317.
- [23] C. Sabathier, J. Chaumont, J.C. Krupa, Dose rate and temperature effects in radiation disorder creation in  $\text{SrTiO}_3$ , *Nucl. Instrum. Methods B* 196 (2002) 308.
- [24] Y. Zhang, J. Lian, C.M. Wang, W. Jiang, R.C. Ewing, W.J. Weber, Ion-induced damage accumulation and electron-beam-enhanced recrystallization in  $\text{SrTiO}_3$ , *Phys. Rev. B* 72 (2005) 094112.
- [25] K.L. Smith, N.J. Zaluzec, G.R. Lumpkin, In situ studies of ion irradiated zirconolite, pyrochlore and perovskite, *J. Nucl. Mater.* 250 (1997) 36.
- [26] R.C. Ewing, A. Meldrum, L.M. Wang, S.X. Wang, Transformation processes in minerals, in: S.A.T. Redfern, M.A. Carpenter (Eds.), *Reviews in Mineralogy and Geochemistry*, vol. 39, Mineralogical Society of America, Washington, DC, 2000.
- [27] M.R. Levy, R. Grimes, Disorder processes in  $\text{A}^3\text{B}^3\text{O}_3$  compounds: implications for radiation tolerance, *Philos. Mag.* 84 (2004) 533.
- [28] K. Trachenko, M. Pruneda, E. Artacho, M.T. Dove, Radiation damage effects in the perovskite  $\text{CaTiO}_3$  and resistance of materials to amorphization, *Phys. Rev. B* 70 (2004) 134112.
- [29] T. Tanaka, R. Nagayasu, F. Sato, T. Muroga, T. Ikeda, T. Iida, Comparison of electrical properties of ceramic insulators under gamma ray and ion irradiation, *Fusion Eng. Des.* 81 (2006) 1027.
- [30] N. Matsunami, T. Shimura, H. Iwahara, Anomalous penetration of implanted deuterium in proton conductive perovskite oxides, *Solid State Ionics* 106 (1998) 155.
- [31] T. Tanaka, A. Suzuki, T. Muroga, F. Sato, T. Iida, T. Nishitani, Radiation induced conductivity of ceramic coating materials under 14 MeV neutron irradiation, *J. Nucl. Mater.* 329–333 (2004) 1434.
- [32] R. Kumar, S.K. Arora, D. Kanjilal, G.K. Mehta, R. Bathe, S.K. Date, S.R. Shinde, L.V. Saraf, S.B. Ogale, S.I. Patil, Swift heavy ion irradiation effects on transport properties of epitaxial thin films of  $\text{La}_{1-x}\text{Ca}_x\text{MnO}_3$ , *Radiat. Eff. Defects Solids* 147 (1999) 187.
- [33] O. Osmani, A. Duvenbeck, E. Akcöltekin, R. Meyer, H. Lebiusand, M. Schleberger, Calculation of electronic stopping power along glancing swift heavy ion tracks in perovskites using *ab initio* electron density data, *J. Phys. Condens. Matter* 20 (2008) 315001.
- [34] E. Akcöltekin, S. Akcöltekin, O. Osmani, A. Duvenbeck, H. Lebius, M. Schleberger, Swift heavy ion irradiation of  $\text{SrTiO}_3$  under grazing incidence, *New J. Phys.* 10 (2008) 053007.
- [35] M. Lang, J. Lian, J. Zhang, F.X. Zhang, W.J. Weber, C. Trautmann, R. Neumann, R.C. Ewing, Single-ion tracks in  $\text{Gd}_2\text{Zr}_{2-x}\text{Ti}_x\text{O}_7$  pyrochlore irradiated with swift heavy ions, *Phys. Rev. B* 79 (2009) 224105.
- [36] J. Rodriguez-Carvajal, FullProf 2k, 2001, France.
- [37] M. Lang, F.X. Zhang, J. Lian, C. Trautmann, Z. Wang, R.C. Ewing, Structural modifications of  $\text{Gd}_2\text{Zr}_{2-x}\text{Ti}_x\text{O}_7$  pyrochlore induced by swift heavy ions: disordering and amorphization, *J. Mater. Res.* 24 (2009) 1322.
- [38] W.J. Weber, N.J. Hess, Ion beam modification of  $\text{Gd}_2\text{Ti}_2\text{O}_7$ , *Nucl. Instrum. Methods Phys. Res. B* 80/81 (1993) 1245.
- [39] G.R. Lumpkin, M. Colella, K.L. Smith, R.H. Mitchell, A.O. Larsen, in: I.G. McKinley, C. McCombie (Eds.), *Scientific Basis for Nuclear Waste Management XXI*, vol. 506, Mater. Res. Soc. Symp. Proc., Materials Research Society, Pittsburgh, PA, 1998.
- [40] W.J. Weber, Models and mechanisms of irradiation-induced amorphization in ceramics, *Nucl. Instrum. Methods Phys. Res. B* 166 (2000) 98.
- [41] W.X. Li, L.M. Wang, M. Lang, K. Sun, C. Trautmann, R.C. Ewing, Thermal annealing of latent tracks in apatite and zircon, *Earth Planet. Sci. Lett.* 302 (2011) 227.
- [42] B. Afra, M. Lang, J.M. Zhang, M. Rodriguez, R. Giulian, N. Kirby, R.C. Ewing, C. Trautmann, P. Kluth, Annealing kinetics of latent tracks in Durango apatite measured by small angle X-ray scattering, *Phys. Rev. B* 83 (2011) 064116.
- [43] N.L. Ross, T.D. Chaplin, Compressibility of  $\text{CaZrO}_3$  perovskite: Comparison with Ca-oxide perovskites, *J. Solid State Chem.* 172 (2003) 123.
- [44] H. Mitamura, S. Matsumoto, K.P. Hart, T. Miyazaki, E.R. Vance, Y. Tamura, Y. Togashi, T. White, Aging effects on curium-doped titanate ceramic containing sodium-bearing high-level nuclear waste, *J. Am. Ceram. Soc.* 75 (1992) 392.
- [45] A.J.C. Wilson, Variance apparent Particle sizes for cylinders, prisms and hemispheres, *J. Appl. Crystallogr.* 2 (1961) 181.
- [46] J.I. Langford, D. Louer, Diffraction line profiles and Scherrer constants for materials with cylindrical crystallites, *J. Appl. Crystallogr.* 15 (1982) 20.
- [47] Microstrains are thought to generate Gaussian line profiles while size broadening leads to Lorentzian line shapes, The negligible size broadening in this work corroborates the use of Gaussian profiles.
- [48] S. Ogata, J. Li, N. Hirotsaki, Y. Shibutani, S. Yip, Ideal shear strain of metals and ceramics, *Phys. Rev. B* 70 (2004) 104104.